Label-free and charge-sensitive dynamic imaging of lipid membrane hydration on millisecond time scales

Orly B. Tarun[a,b,c], Christof Hannesschläger[d], Peter Pohl[d], and Sylvie Roke[a,b,c,1]

[a]Laboratory for Fundamental BioPhotonics, Institute of Bioengineering, School of Engineering, École Polytechnique Fédérale de Lausanne, CH-1015 Lausanne, Switzerland; [b]Institute of Materials Science, School of Engineering, École Polytechnique Fédérale de Lausanne, CH-1015 Lausanne, Switzerland; [c]Lausanne Centre for Ultrafast Science, École Polytechnique Fédérale de Lausanne, CH-1015 Lausanne, Switzerland; and [d]Institute of Biophysics, Johannes Kepler University Linz, A-4020 Linz, Austria

Edited by F. Fleming Crim, University of Wisconsin–Madison, Madison, WI, and approved March 1, 2018 (received for review November 7, 2017)

Biological membranes are highly dynamic and complex lipid bilayers, responsible for the fate of living cells. To achieve this function, the hydrating environment is crucial. However, membrane imaging typically neglects water, focusing on the insertion of probes, resonant responses of lipids, or the hydrophobic core. Owing to a recent improvement of second-harmonic (SH) imaging throughput by three orders of magnitude, we show here that we can use SH microscopy to follow membrane hydration of free-standing lipid bilayers on millisecond time scales. Instead of using the UV/VIS resonant response of specific membrane-inserted fluorophores to record static SH images over time scales of >1,000 s, we SH imaged symmetric and asymmetric lipid membranes, while varying the ionic strength and pH of the adjacent solutions. We show that the nonresonant SH response of water molecules aligned by charge–dipole interactions with charged lipids can be used as a label-free probe of membrane structure and dynamics. Lipid domain diffusion is imaged label-free by means of the hydration of charged domains. The orientational ordering of water is used to construct electrostatic membrane potential maps. The average membrane potential depends quadratically on an applied external bias, which is modeled by nonlinear optical theory. Spatiotemporal fluctuations on the order of 100-mV changes in the membrane potential are seen. These changes imply that membranes are very dynamic, not only in their structure but also in their membrane potential landscape. This may have important consequences for membrane function, mechanical stability, and protein/pore distributions.

water | membranes | second-harmonic imaging | lipids | surface potential

The properties of membranes around cells and organelles are critically determined by the structural and dynamical properties of lipid membranes (1, 2). The distribution of charge, chemical composition, and presence or absence of domains at membranes determine the traffic in and out of cells, the structural integrity, and the response of cells to their environment, even leading to cell death (3). In addition, the hydration of lipid membranes is key to their structural integrity: Without water, lipids will not self-assemble into a membrane structure or remain stable. Imaging membrane hydration, the dynamics of charge, lipid domain formation, and diffusion is a formidable challenge relevant for understanding membrane properties and utilizing them for treating related diseases, such as neurodegenerative disorders (4). Owing to the importance of membranes, a wide variety of imaging methods are used that are either geared toward measuring the fate of membrane-inserted probes and their relation with the membrane, such as confocal fluorescence microscopy (5, 6), stimulated emission depletion far-field fluorescence nanoscopy (7), and superresolution fluorescence imaging (8), or to probe the resonant response, using coherent anti-Stokes Raman scattering microscopy (9–11), or stimulated Raman scattering microscopy (12). Refractive index contrast or the height difference of the hydrophobic core of the membrane that are substrate-dependent are also employed in methods such as interferometric scattering microscopy (13), ellipsometry (14), and atomic force microscopy (15, 16). Second-harmonic (SH) and sum frequency (SF) generation have been recognized as powerful probes of membrane function: The intrinsic symmetry selection rule that applies to both methods ensures that centrosymmetric structures such as ideal single-component lipid bilayers do not emit SH or SF photons. With this in mind, the vibrational response of lipids in supported lipid membranes was used to spectroscopically probe transmembrane lipid motion (17) and lipid acyl chain conformation in monolayers on air/water interfaces (18). SH imaging studies have been performed on lipid bilayers deposited on a substrate in which the UV resonance of specific drugs or chiral molecules was employed to record static structural maps (19, 20). Another study employed static SH imaging to confirm single-component membrane symmetry and relate it to the stability of black lipid membranes formed with different substrates (21). Due to the weak nonlinear optical response in these experiments, recording times are more than 20 min per image. Since structural changes occur on much shorter time scales, no dynamic information has been obtained.

The above methods have greatly advanced membrane research, but have so far ignored the hydrating water, without which membranes cannot exist (22, 23). Recently, we demonstrated high-throughput wide-field SH imaging (24, 25) where we

Significance

Lipid bilayer membranes are responsible for compartmentalization, signaling, transport, and flow of charge in living cells. Membranes self-assemble in aqueous solutions. Without a hydrating environment, membranes cannot exist. It is therefore surprising to note that the hydrating water is neglected in most membrane-related studies. We imaged membrane-bound oriented water by means of label-free second harmonic microscopy. We tracked, on millisecond time scales, membrane domain diffusion of condensed charged lipid domains, domain structure, and the spatial distribution of charge. Real-time electrostatic membrane potential maps were constructed using nonlinear optical theory. The spatiotemporal fluctuation in the membrane potential is surprisingly large and reveals the importance of charge fluctuations on membranes.

Author contributions: O.B.T., P.P., and S.R. designed research; O.B.T. and C.H. performed research; O.B.T., C.H., P.P., and S.R. analyzed data; and O.B.T. and S.R. wrote the paper.

The authors declare no conflict of interest.

This article is a PNAS Direct Submission.

[1]To whom correspondence should be addressed. Email: sylvie.roke@epfl.ch.

This article contains supporting information online at www.pnas.org/lookup/suppl/doi:10.1073/pnas.1719347115/-/DCSupplemental.

Published online April 2, 2018.

improved the throughput of an SH microscope by a factor of ~5,000 compared with a confocal scanning microscope (25), enabling the measurement of interfacial water that was oriented by the presence of surface charges inside a glass microcapillary. If high-throughput wide-field SH imaging were to be applied to lipid membrane research, it would be possible to image the molecular structure of membrane-interacting water that is interrelated with hydration, the presence of local charges, ionization states, and membrane potentials. Such information, if obtained on a subsecond time scale, would provide a new pathway to image the dynamic molecular response of membranes and relate molecular structure to macroscopic function.

Here, we show that wide-field high-throughput SH imaging can indeed be used to label-free image the water molecules in the hydration shells of charged membranes. As hydrating water molecules are oriented by the ionic groups in the lipid head groups of charged lipids through charge–dipole interactions, they can emit SH photons. We use a series of experiments based on changing the membrane composition, changing the ionic content of the aqueous phase adjacent to both membrane leaflets, and the pH of the solution to demonstrate that the hydrating water can be used to image membrane structure. We then SH image domain diffusion on millisecond time scales in cholesterol (Chol)-rich freestanding lipid membranes by means of the water contrast and show that the diffusion times of whole domains compare well to time scales measured with fluorescence microscopy. Finally, we use the second-order optical response of water to measure the membrane potential and changes therein as a function of an external bias. While the average potential follows the quadratic dependence on an external bias, extractable from nonlinear optical theory, individual images show dynamic spatiotemporal fluctuations on the order of 100 mV.

Results and Discussion

SH Imaging of Membrane Hydration. Freestanding horizontal planar lipid bilayers are formed in an aperture of a thin Teflon film by the apposition of lipid monolayers formed on two different air/water interfaces (20, 26, 27). The presence of a bilayer inside a ~80- to 120-μm-sized circular aperture in a 25-μm-thick Teflon film is confirmed with white-light imaging and electrical recordings (Fig. 1*A* and Fig. S2). The appearance of Newton diffraction rings and the measured specific capacitance (C_m) and specific resistance (R_m) of the membrane ($C_m > 0.7$ μF/cm^2, $R_m \approx 10^8$ Ω·cm^2, Fig. 1*A*) agree well with literature values (26, 27). Compositional transleaflet asymmetry is confirmed by capacitance minimization measurements (28, 29) that are sensitive to differences in surface charge density between the leaflets (*Verification of Transmembrane Asymmetry by Capacitance Minimization*).

The horizontally mounted membranes are sandwiched between pH-neutral aqueous 0.1-mM KCl solutions and are imaged with a medium repetition rate wide-field SH microscope (24) that employs a counterpropagating double-beam geometry

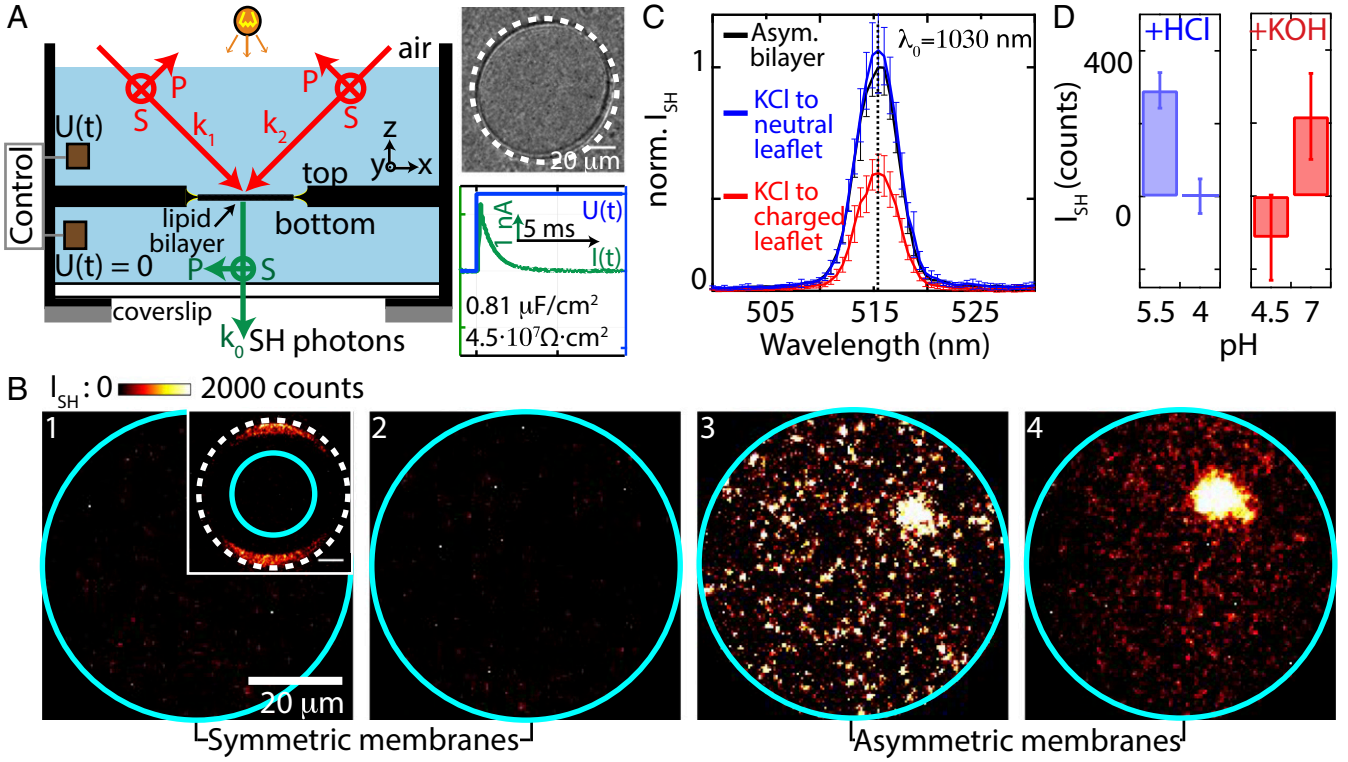

Fig. 1. SH imaging of membrane hydration. (*A*) Two counterpropagating 190-fs beams overlap in space and time to illuminate the membrane. SH photons are collected in the phase-matched direction (see Fig. S3 for details). A white-light image with diffraction rings (indicated by a dashed white circle) and a current response I(t) to a 20-mV bias [*U*(t)] are also shown. (*B*) SH images (20 frames, 560 ms each; magnification: 50×, NA = 0.65) of a symmetric membrane composed of (*1*) 75:25 mol % DOPC:Chol, and (*2*) 37.5:37.5:25 mol % DPPC:DOPC:Chol, and an asymmetric membrane composed of 37.5:37.5:25 mol % DPPS; DOPC:Chol (top leaflet) and 37.5:37.5:25 mol % DPPC:DOPC:Chol (bottom leaflet) (*3*) single frame, and (*4*) average of 20 frames. *Inset* in *B* shows the SH response of the Teflon film where the aperture that contains the bilayer is indicated by the white dashed circle. Analyses are performed only on the central part of the bilayer (cyan circle) as shown in *1*–*4*. The images are collected with all beams P-polarized. (*C*) SH spectra of an asymmetric membrane composed of 70:30 mol % DPhPC:DPhPS (top leaflet) and DPhPC (bottom leaflet), black trace, and after addition of 0.5 mM of KCl to the bottom chamber containing the neutral leaflet [DPhPC + $(KCl)_{aq}$, blue], or the top chamber containing the charged leaflet [DPhPC:DPhPS + $(KCl)_{aq}$, red]. (*D*) Average SH intensity of an asymmetric DPhPS (top leaflet)/DPhPC (bottom leaflet) membrane before (pH = 5.5) and after (pH ≈ 4) addition of $(HCl)_{aq}$ (blue) to the top compartment. Starting at pH = 4.5 and adding $(KOH)_{aq}$ to reach a pH-neutral solution increases the intensity. SH scattering images of a 100-μM KCl solution were subtracted from the raw images. The error bars represent the SDs from 20 spectra (*C*) or images (*D*).

(Fig. 1*A* and Fig. S3). Images are recorded with a numerical aperture (NA) of 0.65 or 0.42, and the SH photons are detected in the phase-matched direction, perpendicular to the membrane position. The polarization combination of the two incoming 1,030-nm, 190-fs, 200-kHz pulses and the emitted 515-nm intensity is controllable. The transverse resolution is 430 nm. For more information on the imaging throughput of the setup, see ref. 24. Fig. 1*B* shows SH images of the central part of several membranes: Fig. 1 *B*, *1* shows a symmetric membrane composed of 75:25 mol % 1,2-dioleoyl-*sn*-glycero-3-phosphocholine (DOPC) and Chol, Fig. 1 *B*, *2* shows a symmetric membrane composed of 37.5:37.5:25 mol % 1,2-dipalmitoyl-*sn*-glycero-3-phosphocholine (DPPC), DOPC, and Chol in which domains of a more ordered phase composed of primarily saturated acyl chain lipids are formed within a more liquid phase consisting of primarily unsaturated lipids, and Fig. 1 *B*, *3* and *4* shows an asymmetric membrane composed of 37.5:37.5:25 mol % 1,2-dipalmitoyl-*sn*-glycero-3-phospho-L-serine (DPPS), DOPC, and Chol (top leaflet) and 37.5:37.5:25 mol % DPPC, DOPC, and Chol (bottom leaflet) that also displays domain formation. The acquisition time for each image was 560 ms, and Fig. 1 *B*, *4* represents an average of 20 frames. The images were collected with all beams P-polarized. Fig. 1 *B*, *1*, *Inset* displays an SH image recorded from the Teflon film, where the aperture that contains the bilayer is indicated by the white dashed circle. It can be seen that SH photons appear from the edge of the Teflon aperture but not from the center of the membrane. The absence of SH photons from the center of a symmetric bilayer arises from the fact that oppositely oriented polar molecules do not emit SH photons [within the dipole approximation (30)]. This result agrees with the images obtained by Ries et al. (21). As the membrane is ∼5 nm thick in the center of the aperture, while the Teflon film is 25 μm thick, there is only a bilayer membrane inside the cyan circle. Outside the cyan circle, but still inside the white dashed circle (the aperture), there is a mixture of hexadecane oil covered with lipids. This curved membrane around the edges of the Teflon film emits SH photons, because, with increasing distance between opposing curved leaflets, there is not anymore destructive interference between the emitted SH photons. This interference process is comparable to observing the emission of SH photons from nanoscopic particles in solution (31). The SH emission from the curved water/lipid/oil edges of the film becomes brighter for larger distances between the opposing leaflets. The Teflon ring itself emits a weak two-photon fluorescence.

Comparing the center of symmetric and asymmetric membranes, Fig. 1*B* shows that only the asymmetric membrane generates a clear SH bilayer contrast. Note that the only difference in composition between Fig. 1 *B*, *2* and Fig. 1 *B*, *3* and *4* is that the charge-neutral DPPC in one leaflet is replaced with charged DPPS. This results in the appearance of μm size domains rich in DPPS lipids. The polarization and symmetry selection rules (30, 31) for nonresonant SH generation dictate that centrosymmetric systems (such as an isotropic liquid) will not generate coherent SH photons. Orientational ordering of asymmetric molecules along the surface normal are responsible for the contrast, and will be most pronounced in the PPP polarization combination (30). This is essentially what we observe in Fig. 1*B*: only the asymmetric bilayer generates a SH image, while the symmetric bilayers do not, in agreement with literature (22, 32). Fig. S7 shows that the nonzero polarization combinations are PPP and SSP, with the first (second and third) letter describing the outgoing (incoming) beam(s). These combinations are to be expected for an azimuthally isotropic interface in contact with centrosymmetric media (30). This behavior is distinctly different from fluorescence.

Fig. 1*C* displays the SH spectrum (black) obtained from an asymmetric membrane composed of 1,2-diphytanoyl-*sn*-glycero-3-phospho-L-serine (DPhPS) (top leaflet) and 1,2-diphytanoyl-*sn*-glycero-3-phosphocholine DPhPC (bottom leaflet), which confirms that, indeed, SH light is detected. Candidates for the emission of SH photons are all noncentrosymmetrically structured molecular groups (30, 33), that is, lipids or water. Taking into account the number density difference between water and lipids and previous nonresonant SH scattering studies of liposomes (34, 35), it is likely that the dominant contribution to the SH intensity will be from water. To test this hypothesis, we added 0.5 mM KCl to the solution. Adding KCl changes the ion distribution inside the interfacial electric double layer and modifies the surface potential (36). This modification alters the number of noncentrosymmetrically distributed water molecules that generate SH light (37), but not the number of noncentrosymmetrically distributed lipids. Fig. 1*C* shows that adding KCl to the neutral side of the membrane leads to a negligible difference within error of the measurement in the SH intensity (blue spectrum) (38). Increasing the KCl concentration on the side with the charged leaflet, however, reduces the SH intensity (red spectrum). Thus, the SH response originates primarily from the hydrating water in the electric double layer that is associated with the charged lipid head groups. This interpretation is further confirmed by protonating/deprotonating the asymmetrically distributed DPhPS lipids ($pK_a \approx 5.5$ to 6, at low ionic strength) (3, 39) as shown in Fig. 1*D*. Starting with a bilayer in contact with a pH = 5.5 solution, the ionic strength (I) is 100 μM, which has ∼20 to 50% of the PS groups charge neutral and the other part negatively charged; adding $(HCl)_{aq}$ ($I \approx 130$ μM) leads to a removal of the surface charges and results in a vanishing SH intensity. On the other hand, starting with a membrane in contact with an acidic solution (pH = 4.5, I = 100 μM, all PS groups charge neutral) increasing the pH to ∼7 ($I \approx 130$ μM) by adding $(KOH)_{aq}$ ionizes most of the PS groups and results in a sharp increase in the SH intensity, which is indeed the case.

Having determined that the hydrating water associated with charged lipids is responsible for the SH emission of asymmetric lipid bilayers, we proceed to use the orientational order of water around charged head groups as a label-free and in situ probe of membrane dynamics.

SH Imaging of Membrane Structure and Dynamics. To image membrane dynamics in real time, an asymmetric membrane of the same composition as used in Fig. 1 *B*, *3* is formed at elevated temperatures (>60 °C) which is then cooled down to room temperature. Ternary mixtures of lipids with different transition temperature, degree of saturation, and chain length (e.g., DPPS vs. DOPC), mixed with Chol, phase separate into liquid-ordered (rich in DPPS with Chol) and liquid-disordered (rich in DOPC) phases (40–43). To verify phase separation, we labeled the charged leaflet (DPPS/DOPC/Chol) with TopFluor Chol that is known to partition into the Chol-rich hydrophobic phase (44, 45) and imaged the membrane two-photon exited fluorescence with 110-ms acquisition time. Fig. 2*A* shows ∼3-μm-diameter domains of a liquid-ordered DPPS-rich phase. Mean square displacement (MSD) traces (orange) are shown in Fig. 2*C*, with a diffusion constant of $D = 0.19 \pm 0.01$ $\mu m^2/s$, in agreement with literature (41). Fig. 2*B* shows an SH image recorded with 180-ms acquisition time of a membrane with the same composition, but now following the hydrating water around the charged head groups of DPPS, label-free. Domains with a similar size and diffusion speed (Fig. 2*C*, green, $D = 0.23 \pm 0.06$ $\mu m^2/s$) are observed. Corresponding movies are shown in *Supporting Information*. Although both imaging modalities measure a different observable, the presence of fluorophores attached to modified Chol inserted in the condensed phase vs. the hydrating water in contact with the head groups of charged DPPS lipids in the condensed phase, the similarity between the fluorescently labeled membrane images and the nonlabeled membrane SH images suggests that it is indeed possible to probe membrane dynamics by means of the hydration shells of the charged lipids.

Having shown that membrane hydration can be tracked dynamically and label-free, we proceed to use the charge-induced

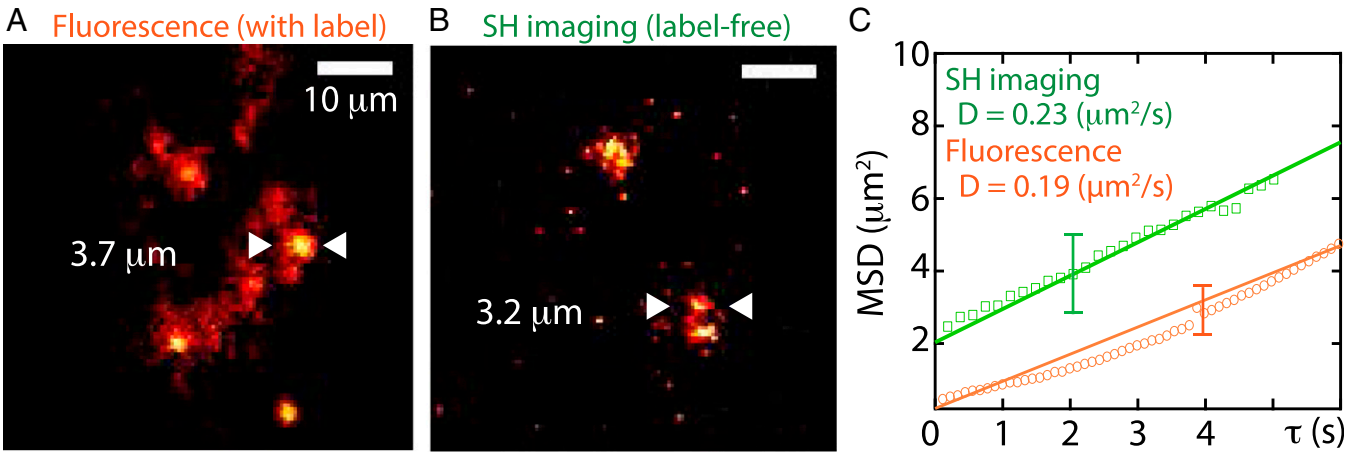

Fig. 2. SH imaging of water around liquid-ordered domains of charged lipids. (*A*) Fluorescence image of an asymmetric membrane composed of 37.5:37.5:25 mol % DPPS/DOPC/Chol + TopFluor (top) and 37.5:37.5:25 mol % DPPC/DOPC/Chol (bottom). (*B*) SH image of a membrane made with the same composition and asymmetry but now label-free. (Scale bar, 10 μm.) The arrows in *A* and *B* point to the positions where the line profiles were obtained to extract the domain size. Both images show phase separation, leading to DPPS and Chol-rich domains of similar size. (*C*) MSD as a function of delay time (τ) comparing label-free SH imaging with TopFluor labeled imaging. The calculated diffusion coefficients are comparable. SH scattering images of a 100-μM KCl solution were subtracted from the raw SH images. Symbols are experimental data and lines are linear fits. More data recorded on longer time scales are shown in Fig. S4.

orientational order of water molecules to derive membrane potentials. Changes in the membrane potential are induced by external stimuli.

Membrane Potential SH Imaging. The electrical activity in membranes underlies a wide variety of chemical and physical processes in cells: the contraction of muscle cells, the communication of neurons, and transport functions all depend on membrane potentials (3). To date, lipid bilayer membrane potentials cannot be imaged directly and noninvasively, and the method below provides a proof of the possibility to do this label-free and in real time. SH measurements and theoretical considerations have shown that the SH intensity of an

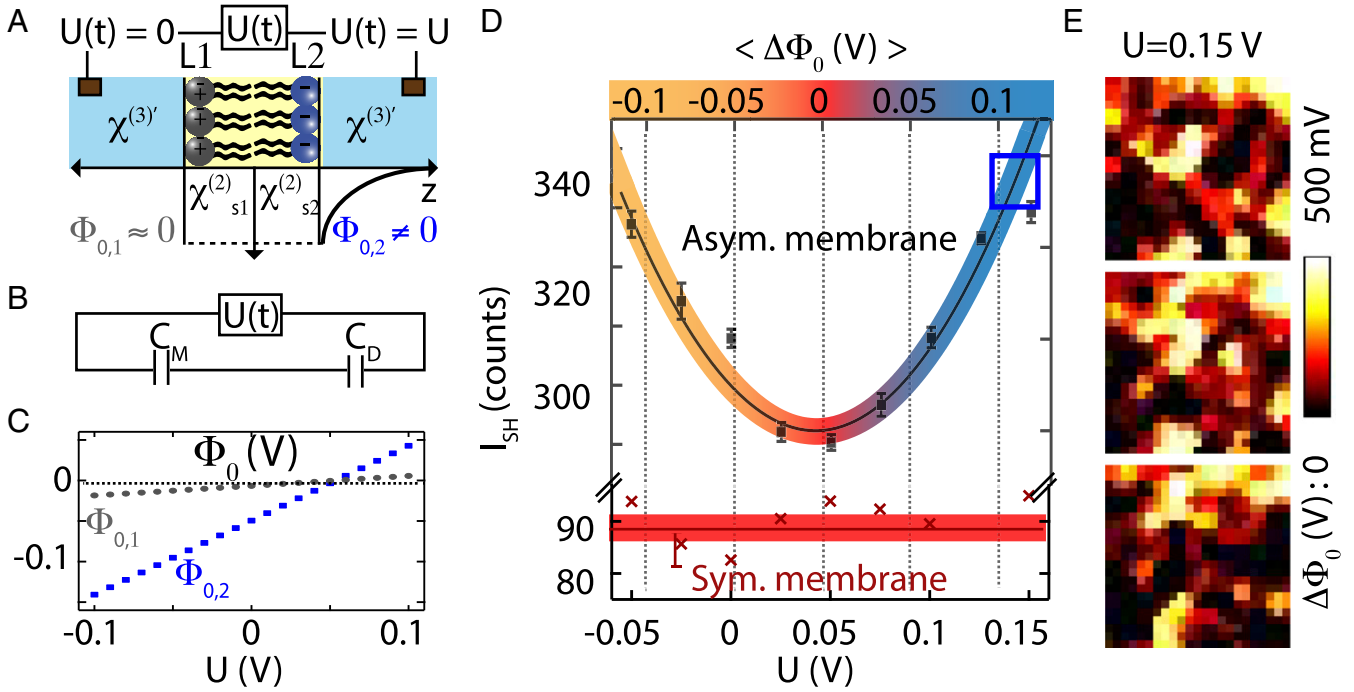

Fig. 3. Voltage-sensitive SH imaging of the changes in membrane surface potential. (*A*) Illustration of the membrane with one neutral (L1) and one charged (L2) leaflet, the susceptibility ($\chi_s^{(2)}$ and $\chi^{(3)\prime}$), and surface potential Φ_0. (*B*) Simplified model of a membrane with capacitance C_m in series with a double layer of capacitance C_D. (*C*) One-dimensional COMSOL simulation of the shift in surface potential as a function of an applied bias for an asymmetric membrane (see *Numerical Computations* for details); $\Phi_{0,1}/\Phi_{0,2}$ shows the linear response of the surface potential of the neutral and charged leaflet as a function of external bias (*U*). (*D*) Spatially averaged SH intensities per pixel as a function of an applied bias (*U*) for an asymmetric membrane composed of 70:30 mol % of DPhPC:DPhPS (top leaflet) and DPhPC (bottom leaflet) (black data), and a symmetric membrane composed of DPhPC (dark red data). The top axis shows the average surface potential changes for the corresponding applied bias, with the coloring corresponding to the average surface potential changes. The average intensity values were computed over a 25-μm-diameter aperture. SH scattering images of a 100-μM KCl solution were subtracted from the raw images. The error bars represent the SD of the mean from 20 images. (*E*) Surface potential maps for three subsequent frames, 2-s acquisition time, with an external bias of 150 mV. The maps are taken from the central part of the membrane 23 μm × 23 μm in size.

interface depends on the surface potential (Φ_0) via $I(2\omega) \approx \left|\chi_s^{(2)} + \chi^{(3)'}\Phi_0\right|^2$ (37, 46), where $\chi_s^{(2)}$ is the surface second-order susceptibility and $\chi^{(3)'}$ is an effective third-order susceptibility of the aqueous phase (see refs. 34 and 47 for more details). For our imaging experiment, there are two oppositely oriented membrane interfaces i, that each have a surface potential $\Phi_{0,i}(x,y)$ (Fig. 3*A*, top) resulting in

$$I(2\omega,x,y) \approx I(\omega,x,y)^2 \Big| \chi_{s1}^{(2)}(x,y) - \chi_{s2}^{(2)}(x,y) + \chi^{(3)'} f_3 \left(\Phi_{0,1}(x,y) - \Phi_{0,2}(x,y)\right)\Big|^2, \quad [1]$$

where f_3 is an interference term which has the form factor $f_3 = \kappa/\kappa - i\Delta k_z$, containing Δk_z as the wave vector mismatch ($\Delta k_z = |\boldsymbol{k}_{1z} + \boldsymbol{k}_{2z} - \boldsymbol{k}_{0z}| = k_{1z} + k_{2z} + k_{0z}$, and $\boldsymbol{k}_{1,2}$ as the incoming wave vectors and $\boldsymbol{k}_0$ as the outgoing wave vector), and κ as the inverse Debye length. This term describes interference effects within the electric double layer. For the transmission experiment employed here, $f_3 \to 1$ (47). Fig. 3*A* shows a schematic of an asymmetric membrane subject to an external bias U. The effect of an external bias U can be simplified by treating the membrane as a capacitor (C_m) in series with the electric double layer approximated as a capacitor (C_D) with a plate spacing equal to the Debye length ($1/\kappa$) as shown in Fig. 3*B*. The specific capacitance ($C_D = \varepsilon_0\varepsilon_r\kappa$) of the double layer is then ~2.3 μF/cm^2 using ε_r = 80, and $1/\kappa$ = 30.3 nm (corresponding to I = 100 μM). Applying an external bias U to the membrane (C_m = 0.7 μF/cm^2) in series with the double layer (Fig. 3*B*), 23% of the potential drop occurs in the double layer. This modifies the ion concentration near the membrane, and changes the surface potential (Fig. 3*C*), such that $\Delta\Phi_0(U) = \Delta\Phi_{0,\mathrm{ini}} + \beta U$ with β a constant of proportionality and $\Delta\Phi_{0,\mathrm{ini}}$ the initial surface potential difference at zero external bias ($U = 0$). Fig. 3*C* shows an estimate of the proportionality relation between Φ_0 and U derived from a COMSOL simulation (COMSOL Multiphysics software) for an asymmetric bilayer (*Numerical Computations*). The surface potential of each leaflet changes as a function of bias, with the majority of the change occurring in the charged leaflet. For a symmetric zwitterionic membrane, from Eq. **1**, we have $\chi_{s1}^{(2)} = \chi_{s2}^{(2)}$ and $\Phi_{0,1} = \Phi_{0,2} = 0$, resulting in a vanishing response (Fig. 1 *B*, *I* and Fig. 3*D*, dark red). For an asymmetric membrane with charge neutral leaflet (L1, $\Phi_{0,1} \approx 0$) and charged leaflet (L2, $\Phi_{0,2} \neq 0$) (Fig. 3*D*, black), we expect a quadratic dependence of the SH intensity on $\Delta\Phi_0 = \Phi_{0,1} - \Phi_{0,2}$ and thus also on U. When the bias (U) compensates the initial surface potential difference, i.e., $\Delta\Phi_{0,\mathrm{ini}} \approx -\beta U$, $\Delta\Phi_0 \approx 0$, we expect a minimum in the induced surface potential difference and thus a minimum in the recorded SH intensity.

Fig. 3*D* shows the average recorded SH intensity per pixel as a function of bias for a charge-neutral DPhPC symmetric bilayer (dark red), and an asymmetric charged bilayer composed of a 70:30 mol % mixture of DPhPC:DPhPS lipids on the top leaflet and DPhPC on the bottom leaflet (Fig. 3*D*, black). A quadratic dependence of the SH intensity on the applied bias U is observed for the asymmetric membrane but not for the symmetric membrane, consistent with Eq. **1**. To obtain the surface potential changes induced by the bias, the data were fitted using Eq. **1** with $\chi^{(3)'} = -10.3 \times 10^{-22}$ m^2/V^2 as for 1,2-dioleoyl-*sn*-glycero-3-phospho-L-serine (DOPS) and DOPC liposomes from ref. 34, $\chi_{s1}^{(2)} - \chi_{s2}^{(2)} = 5 \times 10^{-24}$ m^2/V corresponding to 3% of the value of $\chi_s^{(2)}$ from a monolayer membrane (34), and the average surface potential difference $\langle\Delta\Phi_0(x,y)\rangle$ as a variable. The retrieved values for $\langle\Delta\Phi_0(x,y)\rangle$ are plotted on the top axis, with the initial surface potential difference $\Delta\Phi_{0,\mathrm{ini}}$ around −50 mV. This value corresponds to 0.6% of ionized lipids (*Numerical Computations*) and is consistent with the theory of charge condensation (35, 48). Fig. 3*E* shows snapshots of the membrane potential recorded for three subsequent frames, 2 s in acquisition time, with an external bias of 150 mV. It can be seen that fluctuations across the membrane occur that change from frame to frame. Although the average membrane potential of the 20-frame data stack is 115 mV, fluctuations as large as ~100 mV are observed. The fluctuations suggest a variable degree of ionization from 0 to ~6% in the images of Fig. 3*E* (using the values from the COMSOL simulation).

It is thus possible to optically determine the membrane surface potential label-free and to track spatiotemporal changes in it as a function of an external bias. The fluctuations imply that membranes are very dynamic, not only in their structure but also in their membrane potential landscape. The fluctuations observed in the membrane potential can arise from the association/dissociation dynamics of surface charges similar to the observed heterogeneous association rates on the surface of silica glass (25). This spatial and temporal heterogeneity could have important consequences for membrane function, mechanical stability, and protein/pore distributions.

Summary and Conclusions

In summary, we have shown, in a series of experiments on free-standing lipid membranes involving symmetric and asymmetric lipid membranes, and changes in the ionic and pH content of adjacent solutions, that hydrating water can be SH imaged on subsecond time scales. This hydrating water has a nonrandom orientation, as it is oriented by the charge−dipole interactions between charged lipid head groups and water dipoles. We demonstrate that this contrast mechanism can be used to probe domain diffusion of DPPS-rich domains. In addition, we used the water response to compute the electrostatic membrane potential, and map its dependence on an externally applied field. Although the average membrane potential follows the quadratic dependence on external bias that is modeled by nonlinear optical theory, individual images show dynamic spatiotemporal fluctuations on the order of ~100 mV. These fluctuations illustrate the dynamic link between the aqueous environment and the lipid membrane that is often forgotten.

This contrast mechanism for label-free SH imaging of membranes can be used to acquire molecular-level understanding of membranes that are due to a number of important processes such as specific ion interactions, membrane (interleaflet) structuring and dynamics, membrane fusion, charge-dependent protein activity, ion pumps/pore structure and activity, surface acid/base reactions, and dynamics of membrane potentials. The imaging method is directly applicable to live neurons, without the need to physically patch the cells, thus possibly providing a future noninvasive and clinically viable method of mapping membrane potentials. The connection between the molecular response of the hydrating water and the structural features present in the images provides a unique connection between molecular-level processes involving water and macroscopic observables.

ACKNOWLEDGMENTS. This work is supported by the Julia Jacobi Foundation, the Swiss National Science Foundation, under Grant 200021-140472, and the Austrian Science Fund, under Grant P23679.

1. Simons K, Vaz WLC (2004) Model systems, lipid rafts, and cell membranes. *Annu Rev Biophys Biomol Struct* 33:269–295.
2. van Meer G, de Kroon AIPM (2011) Lipid map of the mammalian cell. *J Cell Sci* 124: 5–8.
3. Marsh D (2013) *Handbook of Lipid Bilayers* (CRC Press, Boca Raton, FL), 2nd Ed.
4. Jackson JD (1998) *Classical Electrodynamics* (Wiley, New York), 3rd Ed.
5. Veatch SL, Keller SL (2005) Seeing spots: Complex phase behavior in simple membranes. *Biochim Biophys Acta* 1746:172–185.
6. Kress A, et al. (2013) Mapping the local organization of cell membranes using excitation-polarization-resolved confocal fluorescence microscopy. *Biophys J* 105:127–136.
7. Eggeling C, et al. (2009) Direct observation of the nanoscale dynamics of membrane lipids in a living cell. *Nature* 457:1159–1162.

8. Korlach J, Schwille P, Webb WW, Feigenson GW (1999) Characterization of lipid bilayer phases by confocal microscopy and fluorescence correlation spectroscopy. *Proc Natl Acad Sci USA* 96:8461–8466.
9. Potma E, de Boeij WP, van Haastert PJM, Wiersma DA (2001) Real-time visualization of intracellular hydrodynamics in single living cells. *Proc Natl Acad Sci USA* 98: 1577–1582.
10. Rinia HA, Burger KNJ, Bonn M, Mu M (2008) Quantitative label-free imaging of lipid composition and packing of individual cellular lipid droplets using multiplex CARS microscopy. *Biophys J* 95:4908–4914.
11. Li L, Cheng J-X (2008) Label-free coherent anti-Stokes Raman scattering imaging of coexisting lipid domains in single bilayers. *J Phys Chem B* 112:1576–1579.
12. Nguyen TT, Conboy JC (2011) High-throughput screening of drug-lipid membrane interactions via counter-propagating second harmonic generation imaging. *Anal Chem* 83:5979–5988.
13. de Wit G, Danial JSH, Kukura P, Wallace MI (2015) Dynamic label-free imaging of lipid nanodomains. *Proc Natl Acad Sci USA* 112:12299–12303.
14. Howland MC, Szmodis AW, Sanii B, Parikh AN (2007) Characterization of physical properties of supported phospholipid membranes using imaging ellipsometry at optical wavelengths. *Biophys J* 92:1306–1317.
15. Shim S-H, et al. (2012) Super-resolution fluorescence imaging of organelles in live cells with photoswitchable membrane probes. *Proc Natl Acad Sci USA* 109:13978–13983.
16. Mashaghi A, et al. (2014) Label-free characterization of biomembranes: From structure to dynamics. *Chem Soc Rev* 43:887–900.
17. Liu J, Conboy JC (2004) Direct measurement of the transbilayer movement of phospholipids by sum-frequency vibrational spectroscopy. *J Am Chem Soc* 126:8376–8377.
18. Roke S, Schins J, Müller M, Bonn M (2003) Vibrational spectroscopic investigation of the phase diagram of a biomimetic lipid monolayer. *Phys Rev Lett* 90:128101.
19. Liu B, et al. (2015) Label-free spectroscopic detection of membrane potential using stimulated Raman scattering. *Appl Phys Lett* 106:173704.
20. Horner A, Akimov SA, Pohl P (2013) Long and short lipid molecules experience the same interleaflet drag in lipid bilayers. *Phys Rev Lett* 110:268101.
21. Ries RS, Choi H, Blunck R, Bezanilla F, Heath JR (2004) Black lipid membranes: Visualizing the structure, dynamics, and substrate dependence of membranes. *J Phys Chem B* 108:16040–16049.
22. Kriech MA, Conboy JC (2005) Imaging chirality with surface second harmonic generation microscopy. *J Am Chem Soc* 127:2834–2835.
23. Dissalvo AE (2015) *Membrane Hydration the Role of Water in the Structure and Function of Biological Membranes* (Springer, Heidelberg).
24. Macias-Romero C, et al. (2014) High throughput second harmonic imaging for label-free biological applications. *Opt Express* 22:31102–31112.
25. Macias-Romero C, Nahalka I, Okur HI, Roke S (2017) Optical imaging of surface chemistry and dynamics in confinement. *Science* 357:784–788.
26. Montal M, Mueller P (1972) Formation of bimolecular membranes from lipid monolayers and a study of their electrical properties. *Proc Natl Acad Sci USA* 69:3561–3566.
27. Gutsmann T, Heimburg T, Keyser U, Mahendran KR, Winterhalter M (2015) Protein reconstitution into freestanding planar lipid membranes for electrophysiological characterization. *Nat Protoc* 10:188–198.
28. Alvarez O, Latorre R (1978) Voltage-dependent capacitance in lipid bilayers made from monolayers. *Biophys J* 21:1–17.
29. Peterson U, et al. (2002) Origin of membrane dipole potential: Contribution of the phospholipid fatty acid chains. *Chem Phys Lipids* 117:19–27.
30. van Meer G, Voelker DR, Feigenson GW (2008) Membrane lipids: Where they are and how they behave. *Nat Rev Mol Cell Biol* 9:112–124.
31. Roke S, Gonella G (2012) Nonlinear light scattering and spectroscopy of particles and droplets in liquids. *Annu Rev Phys Chem* 63:353–378.
32. Smolentsev N, Lütgebaucks C, Okur HI, de Beer AGF, Roke S (2016) Intermolecular headgroup interaction and hydration as driving forces for lipid transmembrane asymmetry. *J Am Chem Soc* 138:4053–4060.
33. Bersohn R, Pao YH, Frisch HL (1966) Double-quantum light scattering by molecules. *J Chem Phys* 45:3184–3198.
34. Lütgebaucks C, Gonella G, Roke S (2016) Optical label-free and model-free probe of the surface potential of nanoscale and microscopic objects in aqueous solution. *Phys Rev B* 94:195410.
35. Lütgebaucks C, Macias-Romero C, Roke S (2017) Characterization of the interface of binary mixed DOPC:DOPS liposomes in water: The impact of charge condensation. *J Chem Phys* 146:044701.
36. Hunter RJ (2001) *Foundations of Colloid Science* (Oxford Univ Press, Oxford).
37. Ong S, Zhao X, Eisenthal K (1992) Polarization of water molecules at a charged interface: Second harmonic studies of the silica/water interface. *Chem Phys Lett* 191: 327–335.
38. Okur HI, Kherb J, Cremer PS (2013) Cations bind only weakly to amides in aqueous solutions. *J Am Chem Soc* 135:5062–5067.
39. Tsui FC, Ojcius DM, Hubbell WL (1986) The intrinsic pKa values for phosphatidylserine and phosphatidylethanolamine in phosphatidylcholine host bilayers. *Biophys J* 49: 459–468.
40. Bakht O, Pathak P, London E (2007) Effect of the structure of lipids favoring disordered domain formation on the stability of cholesterol-containing ordered domains (lipid rafts): Identification of multiple raft-stabilization mechanisms. *Biophys J* 93: 4307–4318.
41. Cicuta P, Keller SL, Veatch SL (2007) Diffusion of liquid domains in lipid bilayer membranes. *J Phys Chem B* 111:3328–3331.
42. Collins MD, Keller SL (2008) Tuning lipid mixtures to induce or suppress domain formation across leaflets of unsupported asymmetric bilayers. *Proc Natl Acad Sci USA* 105:124–128.
43. Boyd RW (2008) *Nonlinear Optics* (Academic, New York), 3rd Ed.
44. Sezgin E, et al. (2012) Partitioning, diffusion, and ligand binding of raft lipid analogs in model and cellular plasma membranes. *Biochim Biophys Acta* 1818:1777–1784.
45. Klymchenko AS, Kreder R (2014) Fluorescent probes for lipid rafts: From model membranes to living cells. *Chem Biol* 21:97–113.
46. Lee CH, Chang RK, Bloembergen N (1967) Nonlinear electroreflectance in silicon and silver. *Phys Rev Lett* 18:167–170.
47. Gonella G, Lütgebaucks C, de Beer AGF, Roke S (2016) Second harmonic and sum-frequency generation from aqueous interfaces is modulated by interference. *J Phys Chem C* 120:9165–9173.
48. Manning GS (2007) Counterion condensation on charged spheres, cylinders, and planes. *J Phys Chem B* 111:8554–8559.